LOI250: Investigation of Metal Ions Drift in Memristive Devices using Perturbed Angular Correlation (PAC) method
Preliminary Results

Student Work Report
Yanik Wettstein
Bsc. Mathematics, ETH Zurich
CERN Summer Student Programme 2023

Supervision: A. Mokhles Gerami, J. Schell, J. G. Correia

September 2023

Abstract

The distinctive electrical characteristics of memristive devices render them an optimal choice for enhancing the computational efficiency of computer systems and facilitating their integration into neuromorphic applications. Particularly noteworthy is their potential application in the field of Artificial Intelligence. This study aims to elucidate the atomic-level structure of memristive devices employing Perturbed Angular Correlation (PAC) spectroscopy. Specifically, our investigation seeks to scrutinize the impact of external voltage on the local electrical field gradients within memristive devices and gain insights into ion channel formation mechanisms.

Our findings underscore the potential of PAC as a promising technique for probing the local structure of memristive devices. However, the examined samples were found unsuitable for PAC measurements, primarily due to the diminutive size of the active zone, which hindered the attainment of statistically significant results. Consequently, we propose an alternative device configuration for future investigations.

Furthermore, our study underscores the critical importance of controlled aging and storage protocols for memristive units, attributable to the formation of silver sulfide on the contact pads of the samples. These insights are pivotal for the development and longevity of memristive device technologies.

Contents

1 Introduction

The memristive devices are introduced conceptually based on symmetry arguments, in 1971 by Leon Chua [3] , as the fourth fundamental electrical circuit element. Chau has proven theoretically that memristive devices do not behave as conventional resistors and their voltage-current relationship is dependent on the past history of applied current or voltage. Although Chua predicted the existence of memristors in 1971, the first particular demonstration has been reported by Hewlett-Packard Labs (HP) [17] in 2008 on thin-film Titanium Dioxide. Nowadays, HP is working on the fabrication of its first 3 nm Memristor crossbar latch memory, which is ten times faster than Dynamic random-access memory (DRAM) [16]. In addition to the operation speed, nano-scale memristive devices are supposed to operate with a lower amount of power compared to the current electronic devices such as metal-oxide-semiconductor (CMOS) [18] transistors.

Generally, memristive devices are classified into two groups based on their resistive switching (RS) effect: volatile and non-volatile switching states [5]. The resistive switching phenomenon refers to the abrupt change in the resistance of devices due to the application of an alternating current pulse. In the volatile switching mechanism, the resistance of the material changes when a high enough voltage or current is applied, but the resistance returns to its initial value when the voltage source has been switched off. In contrast, the resistance in devices with non-volatile resistive switching mechanisms remains unchanged even after eliminating the external current source. Hence, electric devices with non-volatile resistive switching characteristics can be used in the fabrication of long-term memories [4]. Memristor-based non-volatile devices will overcome the current limitation of non-volatile CMOS memory devices. Nowadays, CMOS memory devices have touched Moore's limit and further miniaturization is challenging mainly due to current leakage, power consumption and their complicated geometry (fig. 1), and their switching speed.

In addition to the non-volatile memory applications, memristive devices are expected to revolutionize the future of Artificial Neural Network computation due to their multilevel resistance capability, which made them proficient in mimicking synapses' functionality and routing among neurons [22]. The biological process that a neuron uses to receive a signal from other neurons is shown in (Fig.2). According to the figure, neurons communicate with other neurons by using synapses. Here, biological neurons receive inputs from other neurons through synapses, and synapses trigger an output signal by the combination of the inputs. Memristor arrays might have the same functionality as neural network arrays and therefore, the process can be performed by the hardware, which is much faster compared to traditional software-based calculations. Therefore, improving the efficiency of Memristive devices leads to a considerable impact on the future of Artificial Intelligence.

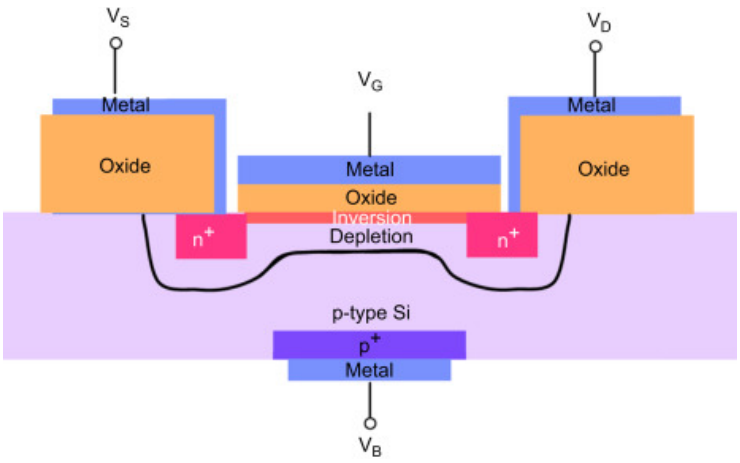

Figure 1: A schematic of the complementary metal-oxide-semiconductor (CMOS) devices [10].

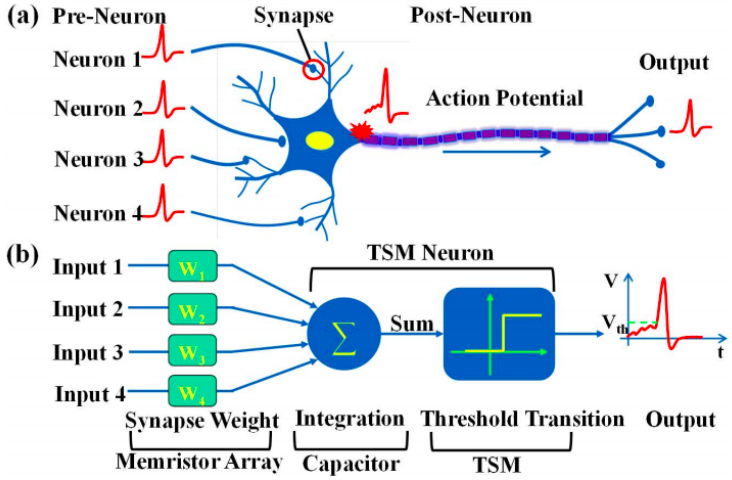

Figure 2: Application of Memristor arrays can play the same functionality in neural network arrays [22]

.

The first experimental observation of the switching mechanism in memristive devices has been reported by HP on $Ag/TiO_2/Pt$ layers[17]. The results indicate that the ON/OFF (SET/RESET) conductance ratio is 1000 for a 50 nm TiO_2 layer [5]. This experiment presents a general model for the switch behavior of the memristive device. According to this model, applying voltage leads to create a metallic channel inside the active insulator layer by moving the positively charged ions dopant (Ag^+) with oxygen vacancies which corresponds to the ON

state. On the other hand, applying reverse voltage moves away vacancies from the active insulator layer which corresponds to OFF state as is shown in Fig. 5

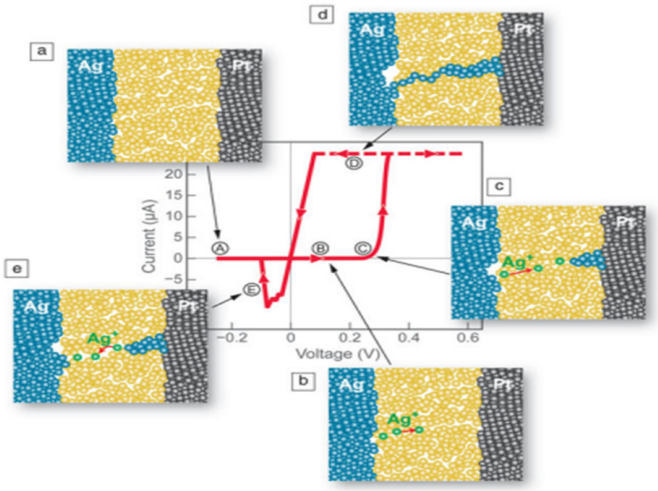

Figure 3: Schematic representation of ion channel formation in $Ag/TiO_2/Pt$ memristive devices, the image was adapted from reference [5]

.

Recently, it is observed that the current-voltage characteristic of non-volatile memristive devices behaves differently depending on the type of material used as an active insulator layer. So that, using simple binary transition metal oxide semiconductors [5, 12] leads to unipolar I-V characteristics as is shown in Fig.4-left . The bipolar I-V characteristic (Fig.4-right) can be achieved by the use of complex oxides compounds [5] such as $YBa_2Cu_3O_{7-x}$ (YBCO), $SrTiO_3$ (STO), Zn-doped amorphous SiO_x (SZO), and also in off-stoichiometry binary oxide. Premiere knowledge on the switching mechanism of memristive devices was presented recently [20, 13]. However, the switching mechanism of Memristor is highly complex, and current knowledge is not sufficient to design and optimize devices to be used in the market. There are several challenges such as improving the reliability, control, and stability of the switching mechanism of devices as well as manufacturing technique [6]. A suitable model is required to elucidate the formation of metallic channels within the active insulator layer and the transition of the device from a high-resistance state (HRS) to a low-resistance state (LRS). Several models have been proposed to explain the migration of metallic channels into the active insulator layer, including valence change memory (VCM), electrochemical metallization (ECM) memory, and thermochemical processes [23, 14]. However, the current understanding of metal ion behavior within the active insulator layer under varying applied voltages remains unclear.

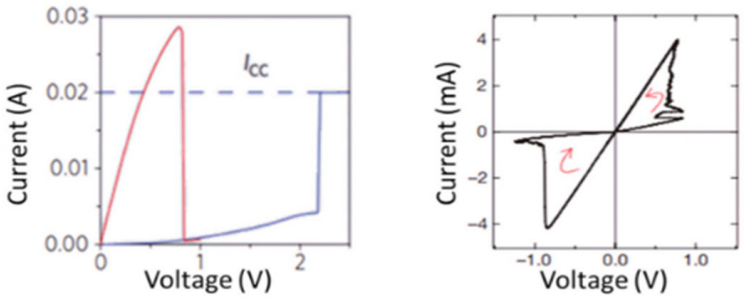

Figure 4: the current vs voltage characteristics of resistive switching in the type of left) unipolar [12] , right) bipolar [5]

.

Addressing these fundamental questions in a systematic manner will facilitate the development of a reliable numerical model for designing memristive devices, ultimately leading to a significant advancement in the construction of novel and highly efficient Memristive devices.
In our current research, we have undertaken a comprehensive study utilizing techniques such as current-voltage measurements (I-V curves) and Perturbed Angular Correlation (PAC) measurements. These investigations aim to shed light on fundamental phenomena, including the observation of defects such as oxygen vacancies, phase transitions, and electronic polarization. For the PAC measurements, donor probes of ^{111m}Cd/^{111}Cd, produced in the mass separator ISOLDE/CERN with an energy of 30keV, were employed.

2 Design of Memristors

The design and fabrication were undertaken by Michaela Blum at TU Ilmenau. The experimental investigation encompassed an analysis of two distinct designs denoted as the "old" and "new" configurations. Both designs comprise a 525 μm silicon substrate, layered successively with a 50 nm SiO_2 layer and a 30 nm TiO_2 layer, upon which platinum and silver electrodes are deposited. A 200 nm layer of silver is applied to both electrodes to enhance the electrical conductivity between the voltage source and the sample electrodes. It is worth noting that only a limited section of the electrodes, characterized by minimal inter-electrode spacing, remains uncoated.
These designs deviate primarily in the geometric arrangement of these electrodes. The coated regions are commonly referred to as contact pads. The new design incorporates four square contact pads, each with dimensions of 1.5 x 1.5 mm^2. The uncoated electrodes form a "V" shape, connecting two contact pads. At their closest proximity, the "V" shaped electrodes maintain a distance of approximately 900 nm.
In contrast, the "old" designs feature two square contact pads, each measuring 3 x 3 mm^2. Each contact pad is linked to a small, uncoated, quadratic electrode measuring 0.1 x 0.1 mm^2, with an inter-electrode gap of 700 nm.

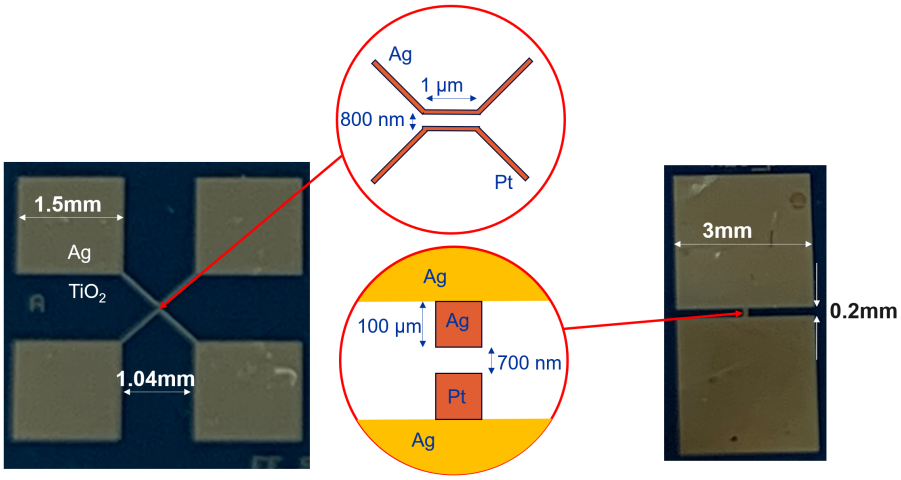

Figure 5: Schematic representation of the two designs. The new design is illustrated on the left and the old design on the right. Design by Michaela Blum at TU Illmenau

.

3 Unperturbed Angular Correlation

The next two sections are primarily based on the Phd. Thesis of M. Nagl [15] and M. Barbosa [1]. Given specific radioactive isotopes such as ^{111m}Cd , which decay is characterised by a γ-γ- cascade. The first photon is emitted during the transition from the initial state (I_i, m_i) with spin I_i and magnetic quantum number m_i to the intermediate state (I, m). The second photon is emitted during the transition from (I, m) to the final and stable ground state (I_f, m_f). The angle between the emitted photons follow a certain distribution given by

$$W(\theta) = 1 + \sum_{k=2}^{k_{max}} A_{kk} P_k(\cos(\theta)) \tag{1}$$

where θ is the angle between the emitted photons, $W(\theta)$ represents the probability to detect the second photon with an angle of θ with respect to the first detected photon. A_{kk} are called angular correlation coefficients and describe the deviation of the isotropic emission. P_k is the k^{th} Legendre Polynomial. Due to selection rules of the transition odd k's are omitted since the angular coefficients have zero value. Further k_{max} is determined by $\min\{2I, L_1 + L_1', L_2 + L_2'\}$ where $L_{1,2}$ and $L'_{1,2}$ are the multipolarities of the transitions. For a more in depth analysis of the computation of the correlation coefficients and a more precise definition of the conditions, which guarantee an an-isotropic radiation pattern the reader is encouraged to read the master thesis of M. Barbosa. [1]

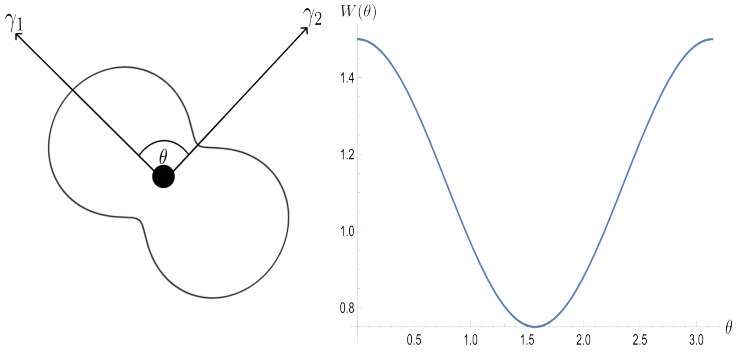

Figure 6: Illustrative representation of the angular correlation.

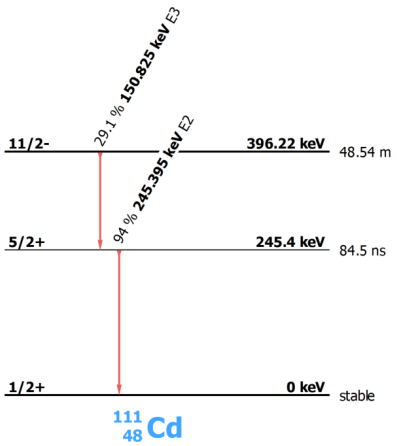

Figure 7: Decay scheme of ^{111m}Cd $\rightarrow^{111}_{48}$Cd drawn by the program Nuclei 2.7 by M. Nagl [15]

4 Perturbed Angular Correlation

The equation (1) is valid if there is no external Magnetic Hyperfine Field or Electric Field Gradient present. Before we discuss the consequences of the presence of such field we first need to define the nuclear magnetic moment and the nuclear quadrupole moment and its interactions with the Magnetic Hyperfine Field and Electric Field Gradient respectively.

4.1 Magnetic Dipole Moment interaction

For this study no magnetic interactions are studied. This chapter is provided for completeness. Let $J(r)$ be a localized distribution of current and $B(r)$ be the magnetic field such that $B(r) = \nabla \times A(r)$ where $A(r)$ is a vector potential. The interaction energy is then given by

$$E_m = -\int J(r) \cdot A(r) d^3r \tag{2}$$

Assuming the magnetic is uniform we can write

$$A(r) = \frac{1}{2} B(r) \times r \tag{3}$$

A proof of this can be found here [2]. Inserting (3) inside (2) we get

$$E_m = -\frac{1}{2} \int (r \times J(r)) \cdot B(r) d^3r \tag{4}$$

Using the classical definition of the magnetic dipolar moment

$$\mu = \frac{1}{2} \int r \times J(r) d^3r \tag{5}$$

we receive the expression for the magnetic dipolar energy

$$E_m = -\mu \cdot B \tag{6}$$

We can also write the dipole moment as the product of the gyromagnetic ratio γ times the angular momentum $\hbar I$

$$\mu = \gamma \hbar I \tag{7}$$

If we choose our z-axis in the direction of the B-field we get

$$E_m = -\gamma \hbar B_z m \tag{8}$$

and hence the energy difference of two neighbouring sub-levels is

$$\Delta E_m = \gamma \hbar B_z = \hbar \omega_L \tag{9}$$

Where we defined $\omega_L = \gamma B_z$. ω_L is also called the Larmor frequency.

4.2 Electric Quadrupole Interaction

Given the nuclear charge distribution $\rho(r)$ and an external electrical potential $\Phi(r)$, the electrical quadrupole interaction energy is defined by

$$E = \int \rho(r)\Phi(r)d^3r. \tag{10}$$

Expanding Φ with the Taylor series around the origin yields

$$\Phi(r) = \Phi(0) + r \cdot \nabla\Phi(0) + \frac{1}{2}\sum_{i,j}\left(\frac{\partial^2\Phi}{\partial x_i \partial x_j}\right)_0 + \dots \tag{11}$$

Using the following definitions:

$$\text{total charge } q = \int \rho(r)d^3r \tag{12}$$

$$\text{electric dipole moment } p_i = \int x_i\rho(r)d^3r \tag{13}$$

$$\text{electric quadrupole moment tensor } Q_{ij} = \frac{1}{e}\int \rho(r)(3x_ix_j - r^2\delta_{ij})d^3r \tag{14}$$

we get

$$E = q\Phi(0) + p \cdot \nabla\Phi(0) + \frac{q}{6}\langle r^2\rangle\nabla^2\Phi(0) + \frac{e}{6}\sum_{ij}\left(\frac{\partial^2\Phi}{\partial x_i \partial x_j}\right)_0 Q_{ij} \tag{15}$$

1. $q\Phi(0)$: constant electrostatic energy
2. $p\cdot\nabla\Phi(0)$: electric dipole interaction. Due to parity reasons of the nuclear wave function this term is zero
3. $\frac{q}{6}\langle r^2\rangle\nabla^2\Phi(0)$: This term is called monopolar term and as we see is only dependent on the nuclear mean square radius $\langle r^2\rangle$. It does not contribute to energy splitting but to a shift of the levels. For a more detailed analysis of the monopolar term the reader is encouraged to have look on G. Schatz book "Nukleare Festkörperphysik". [8]
4. $\frac{e}{6}\sum_{ij}\left(\frac{\partial^2\Phi}{\partial x_i \partial x_j}\right)_0 Q_{ij}$: This term describes the electric quadrupole interaction energy. If the nuclei of interest has a nonnegligible quadrupole moment this term is the most important one regarding energy splitting and the one we are working with.

Write $\left(\frac{\partial^2\Phi}{\partial x_i \partial x_j}\right)_0 =: \Phi_{ij} \Rightarrow \frac{e}{6}\sum_{ij}\Phi_{ij}Q_{ij} = \frac{e}{6}\sum_{ij}M_{ij}$, where M is the Matrix described by $M_{ij} = \Phi_{ij}Q_{ij}$. Using Schwarz' Theorem M is symmetric and hence is diagonizable due to the Spectral Theorem. With out loss of generality we will assume M to be a diagonal 3×3 Matrix where $|V_{zz}| \geq |V_{yy}| \geq |V_{xx}|$.

We can now rewrite $\Phi_{ij} = V_{ij} + \frac{1}{3}\,\mathrm{Tr}\{\Phi''\}$. Where Φ'' is the Matrix $\Phi^3_{i,j=1}$Then $\mathrm{tr}(V) = \sum_{i=1}^{3}\Phi_{ii} - \frac{1}{3}\,\mathrm{Tr}\{\Phi''\} = 0$. Using this definition and tracelessness of Q:

$$\frac{e}{6}\sum_{ij} M_{ij} = \ = \frac{e}{6}\sum_{ii}\left(V_{ii}Q_{ii} + \frac{1}{3}\,\mathrm{Tr}\{\Phi''\}Q_{ii}\right) = \frac{e}{6}\sum_{ii} V_{ii}Q_{ii} \tag{16}$$

We introduce the asymmetry parameter

$$\eta = \frac{V_{yy} - V_{xx}}{V_{zz}} \in [0,1]$$

The corresponding Hamiltonian in quantum formulation is then given by

$$\hat{H}_Q = \frac{eQV_{zz}}{4I(2I-1)}(3\hat{I}_z^2 - I(I+1) + \eta(\hat{I}_x^2 - \hat{I}_y^2)) \tag{17}$$

where Q is the expectation of the Quadrupole Operator $\hat{Q}_{zz}$ and is called Quadrupole Moment. Since we are interested what happens between the emission of the first and the second photon, I is the spin of the nucleus during the intermediate state. For further informations about the energy splitting the reader is encouraged to read Ian Yap's Master Thesis [21]. For $I = \frac{5}{2}$, the hyperfine interaction of the quadrupole moment with the electric field gradient splits the energy level into three sub levels corresponding to the magnetic quantum numbers $m = \pm\frac{5}{2}, \pm\frac{3}{2}, \pm\frac{1}{2}$. The fact that the signs don't matter is due to the squared angular momentum operators $\hat{I}_{x,y,z}$. We define the following frequencies:

1. Quadrupole Frequency: $\omega_Q := \frac{eQV_{zz}}{4I(2I-1)\hbar}$
2. $\nu_Q := \frac{eQV_{zz}}{h}$
3. $\omega_0 = \nu_Q \frac{2\pi k}{4I(2I-1)}$ where $k = 3$ if I is an integer and $K = 6$ if I is the half of an integer.
4. $\omega_1, \omega_2, \omega_3$ are the observable frequencies where ω_1 corresponds to the lowest, and ω_3 to the highest transition frequency.

For axially symmetric electric field gradients ($\eta = 0$):

$$E_Q = \hbar\omega_0(3m^2 - I(I+1)) \tag{18}$$

Thus the energy difference of two sublevels are given by

$$\Delta E_Q = 3\hbar\omega_Q|m^2 - m'^2| \tag{19}$$

The lowest possible non trivial transition frequency for $I = \frac{5}{2}$ is

$$\omega_0 = 3\omega_Q|\frac{3^2}{2^2} - \frac{1^2}{2^2}| = 6\omega_Q = \omega_1$$

Second: $\omega_2 = 12\omega_Q = 2\omega_1$ and third: $\omega_3 = 18\omega_Q = 3\omega_1 = \omega_1 + \omega_2$

4.3 Principles of PAC

While the nucleus is in its intermediate state, the electric quadrupole interaction elicits transitions between the energy levels. These transitions add a time dependent component to equation (1). Since the derivation and even notation of the general expression needs well advanced techniques in quantum theory we will present the result for the special case of the axially symmetric quadrupole interaction ($\eta = 0$) in a poly-crystalline sample with intermediate spin $I = 5/2$:

$$W(\theta, t) = \sum_{k=0}^{k_{max}} A_{kk} G_{kk}(t) P_k(\cos(\theta)) \tag{20}$$

where

$$G_{kk}(t) = \sum_{n=0}^{n_{max}} s_{kn} \cos(n\omega_0 t) \text{ and } n_{max} = \max_{m,m'} \{\frac{1}{2}|m^2 - m'^2|\} \tag{21}$$

s_{kn} are factors dependent of I, m, m' and k. We won't give the details how to calculate s_{kn}. The interested reader is advised to read Lopes' Phd Thesis [11]. Using the approximation $k_{max} = 2$ the expression simplifies to [19]:

$$W(\theta, t) = 1 + A_{22} \frac{1}{5} (1 + \frac{13}{7} \cos(\omega_0 t) + \frac{10}{7} \cos(2\omega_0 t) + \frac{5}{7} \cos(3\omega_0 t)) \frac{1}{2} (3\cos^2(\theta) - 1) \tag{22}$$

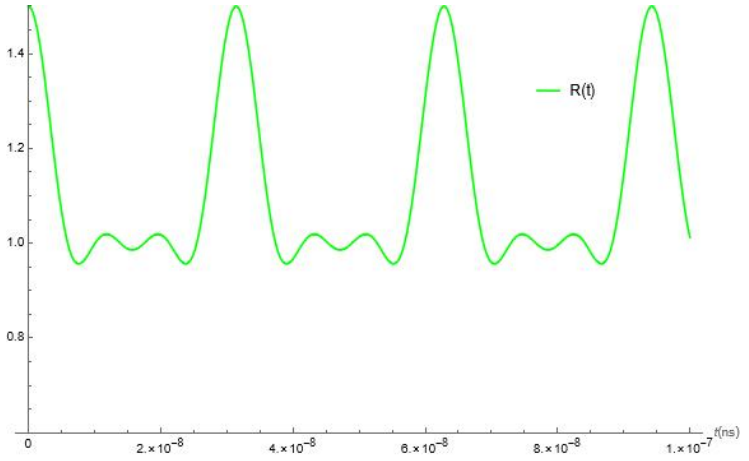

Figure 8: Illustrative plot of $W(\theta, t)$ where $\theta = 0$ and $t \in [0, 100]$ ns, $A_{22} = \frac{1}{2}$

Since radioactive nuclei are implanted the probability of gamma emission is proportional to the exponential decay

$$N_\theta(t) = I_0 W(\theta, t) e^{-\lambda t} \tag{23}$$

where $\lambda = \frac{\ln(2)}{t_{1/2}}$, $t_{1/2}$ is the half-life of the nucleus, I_0 the number of nuclei present. In literature $N_\theta(t)$ is often described as the measured gamma count per detector pair which have angle of θ. In this text we will distinguish between the theoretical value N_θ and the measured value $\hat{N}_\theta$. Neither the exponential decay nor the number of nuclei are of interest but the strength of the electric field gradient. Hence a simple computation is performed in order to cancel the decay rate and the factor I_0. The result is called count ratio and denoted by R and is performed for a setup of detectors where the angles between two detectors are either 180° or 90°:

$$R(t) := 2\frac{N_{180}(t) - N_{90}(t)}{N_{180}(t) + 2N_{90}(t)} \approx A_{22} G_{22}(t) \tag{24}$$

When conducting a real experiment two other things need to be taken in account: First the EFG follows a certain distribution because of course the value is not the exact same at each probe. Second the finite time resolution of the machine is affecting the measured spectrum as well. This can be done by multiplying each G_{kk} term by

$$\underbrace{D(F_{whm}, t)}_{\text{EFG distribution}} \cdot \underbrace{P(F^*_{whm}, \omega_n)}_{\text{finite resolution}}$$

For the distribution of the EFG one usually decides whether it follows a Gaussian distribution:

$$D_{gauss}(F_{whm}, t) = \exp\left(\frac{-F^2_{whm} t^2}{16\ln(2)}\right) \tag{25}$$

or the Lorenzian distribution:

$$D_{lorenz}(F_{whm}, t) = \exp\left(-\frac{F_{whm} t}{2}\right) \tag{26}$$

where F_{whm} is defined over the relation $\sigma = F_{whm}/\sqrt{8\ln 2}$ where σ is the standard deviation of the distribution.

5 Isolde at CERN

The investigated memristive devices in the type of $Pt/TiO_2/Ag$ are studied using PAC measurement by 30 keV ion-implantation of ^{111m}Cd into the devices. When a fast ion passes through matter, it loses energy principally by scattering with electrons within the matter it passes through and, more importantly at low energies, by scattering from the nuclei of the atoms. It may take many atomic layers, before there is a collision with a target atom which is hard enough to stop the incoming ion, by displacing the lattice. The energy required to push the host atom just far enough from its lattice site so that it cannot move back into the created empty site, is the displacement energy. Typical threshold displacement energies in solids are of the order of 10–100 eV. The energy of the incoming ion-beam at ISOLDE/CERN ranges from 30–60 keV resulting in a maximum penetration depth of 500–1000 Å into the memristive devices studied here as demonstrated in Figure 9 by SRIM simulations for the part of implantation in the section layers of TiO_2 and SiO_2.

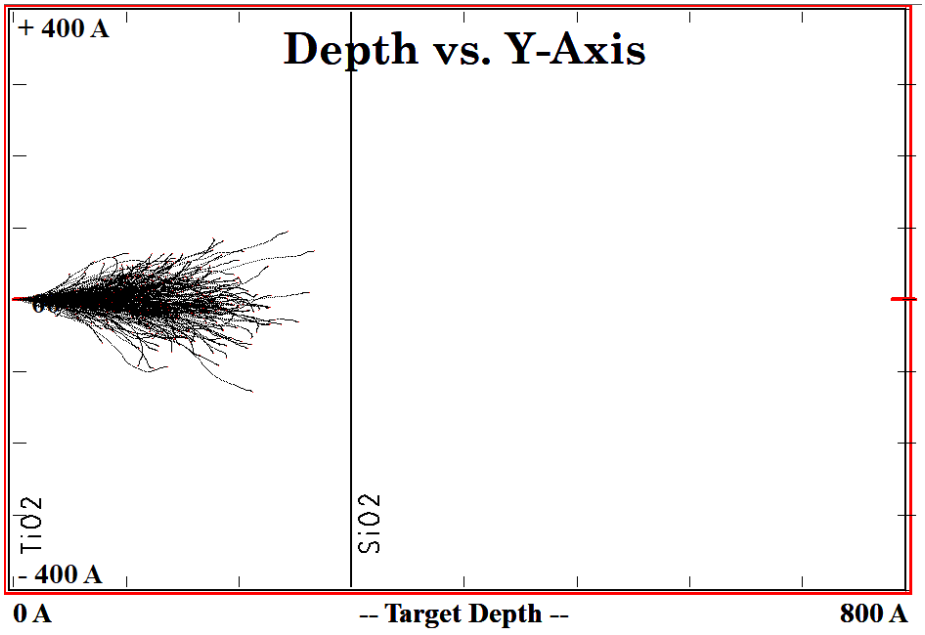

Figure 9: SRIM Simulation for 30nm TiO_2 and 50nm SiO_2

6 Experimental Setup

The two design type ("old" and "new") of Memristive devices of $Ag/TiO_2/Pt$ was used for the implantation
The gap between two electrode on these memristive devices was carefully fixed in the positions of beam spot in the sample holder with clamps and mounted inside the implantation vacuum chamber. The ^{111m} Cd/^{111} Cd with half-life time around $T_{1/2}$ = 48 min was produced online from a molten tin target with a plasma ion source at the ISOLDE/CERN facility and implanted at RT with 30-keV energy and low fluences of 8×10^{10} at/cm^2. Due to the short lifetime of ^{111m} Cd, we carried out an independent cycle of implantation for each measurement. After implantation, the devices have been placed in the center of the planar 4 detector setup "K1" machine as shown in figure 10 for measuring the PAC spectra and current-voltage curve.

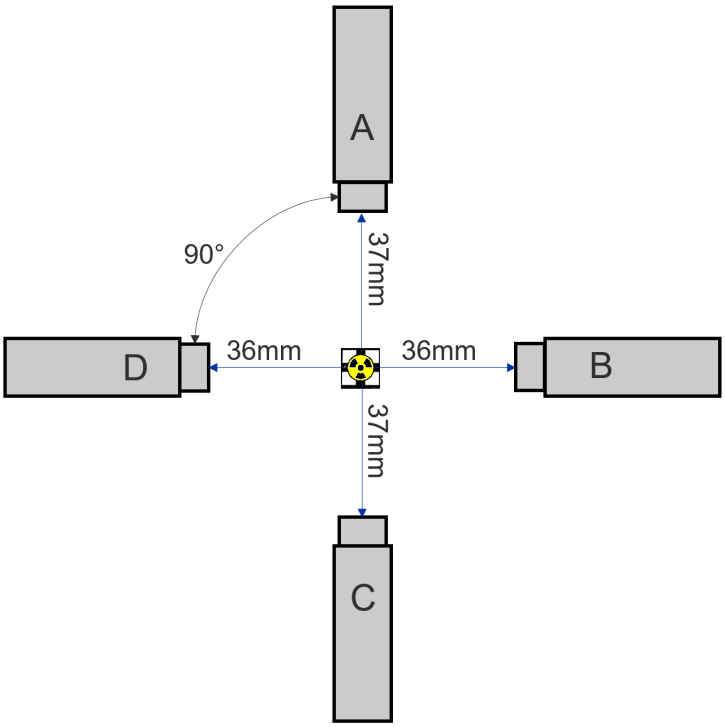

Figure 10: Illustrative representation of K1. A coincidence circuit counted the number of γ-γ emissions per detector pair, for a more detailed description of the coincidence circuit the reader is referred to [15]

There are four detector setup in 90° symmetry. Each detector is able to register both different gammas and so gives start and also stop signals. This leads to eight 90° and four 180°-coincidence spectra. With this start-stop-principle life-

time measurements of the intermediate state are performed, whose exponential decays are temporally modulated due to hyperfine interactions.
After the first implantation, a series of measurements were conducted without applying voltage to the device. In the next step, measurements were taken during the second implantation while voltage was applied to determine the values of forming/switching voltage. Following that, the measurement for the optimized I-V curve was performed. Since the time for applying voltage is limited to each memristive voltage, which is less than the isotope's half-life, we continued the PAC measurement with a voltage of 0 for 3 hours. The experimental setup which is used for applying the voltages is shown in the following figures.

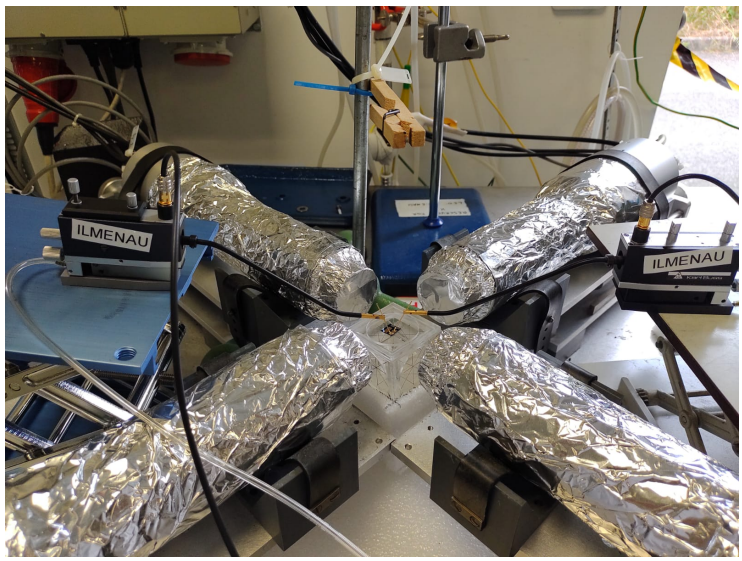

Figure 11: The experimental setup for applying voltage to Memristive devices consists of two manipulators used for applying forces to secure the tips onto the devices. The required voltage range for applying on memristive devices varies from 0 to 100 V, with a limited current value of 10 μA

7 Analysis of PAC Spectroscopy Data

In the context of our measurements, we encountered a need to align the resulting 12 spectra. This alignment was crucial because it involved adjusting the parameter known as t_0, which determines the starting point of each spectrum. The necessity for this adjustment arose due to inherent time shifts introduced by the hardware during data acquisition.
To accomplish this, we employed a specialized program called "Interlude" to synchronize the t_0 values. This program effectively aligned the spectra by utilizing a measurement with minimal errors as a reference point. Subsequently, a parameter file was generated, containing all the relevant data for t_0 alignment. With our t_0 values now synchronized, we proceeded to compute $\hat{R}(t)$ using the above given formula. Where $\hat{N}_{180}, \hat{N}_{90}$ are the geometric mean of the 180 and 90 degrees detector pair spectra respectively. This process, executed by the "Interlude" program, ensured that our measurements were accurately calibrated and ready for further analysis.
The subsequent phase of our analysis involves fitting the theoretical $R(t)$ value to the measured $R(t)$ data. To achieve this, we first establish certain fixed parameters as a foundation before fine-tuning the unknown parameters, namely ω_0, η, δ, and f_1.
The fixed parameters are the following:

Fixed Parameters	
I	2.5
Q	0.664(7) b
A_{22}	0.13630
c_m	0.65

where A_{22} is the corrected angular correlation coefficient which takes the geometry and alignment of the detectors in account. c_m is a multiplication factor to correct uncertainties in the detector setup.
For determination of the unknown parameters GFIT19 a modified version of the NNFIT software package was used. [9] Because of the geometric properties of the "old" samples, the presence of implanted ions within TiO_2 can be considered negligible. As a result, the fitting parameters from the previous samples served as an initial approximation for the gradient descent algorithm implemented in GFIT19, which was used to determine the silver fraction in the "new" samples.

8 Results

8.1 ”old” design samples

Figures 7 and 8 illustrates the recorded $R(t)$ spectra and their corresponding Fourier transforms. In our analysis, we adopted a two-fraction approach to fit the experimental data obtained from the old sample designs. The first fraction predominantly resembles the spectral characteristics of probes implanted within the silver electrodes and contributes approximately 46 to 66% to the overall spectrum. This fraction exhibits notably low central ω_0 frequencies ranging from 2.4 to 4.4 Mrad/s, accompanied by minimal damping. We imposed an axial symmetry parameter of 0 for this fraction, as silver's cubic crystal structure is expected to exhibit a zero electric field gradient. However, the presence of a non-zero frequency suggests the possibility of implantation defects within the silver electrodes.The second fraction demonstrates significantly higher ω_0 frequencies, spanning from 88 to 170 Mrad/s, coupled with pronounced damping. These characteristics cannot be solely attributed to pure silver and constitute a substantial contribution to the observed spectrum. One plausible explanation for this behavior is the corrosion of silver when exposed to atmospheric gases, resulting in the formation of a thin layer of silver sulfide [7]. This phenomenon has been confirmed through Energy Dispersive Spectroscopy (EDX) measurements conducted by Michaela Blum at TU Illmenau, providing a potential explanation for the origin of the second fraction.

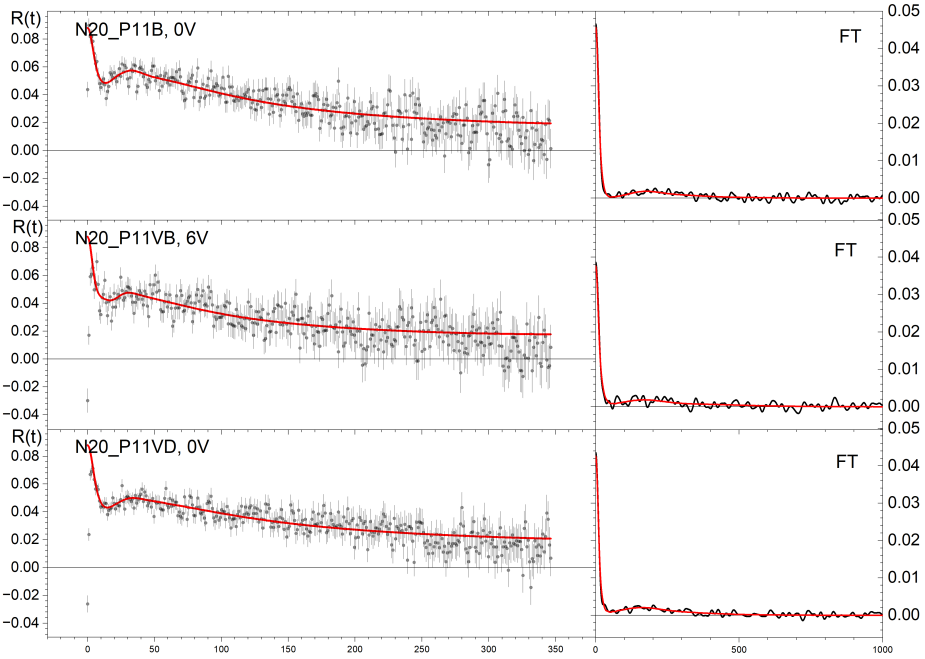

Figure 12: Results of Sample N20_P11

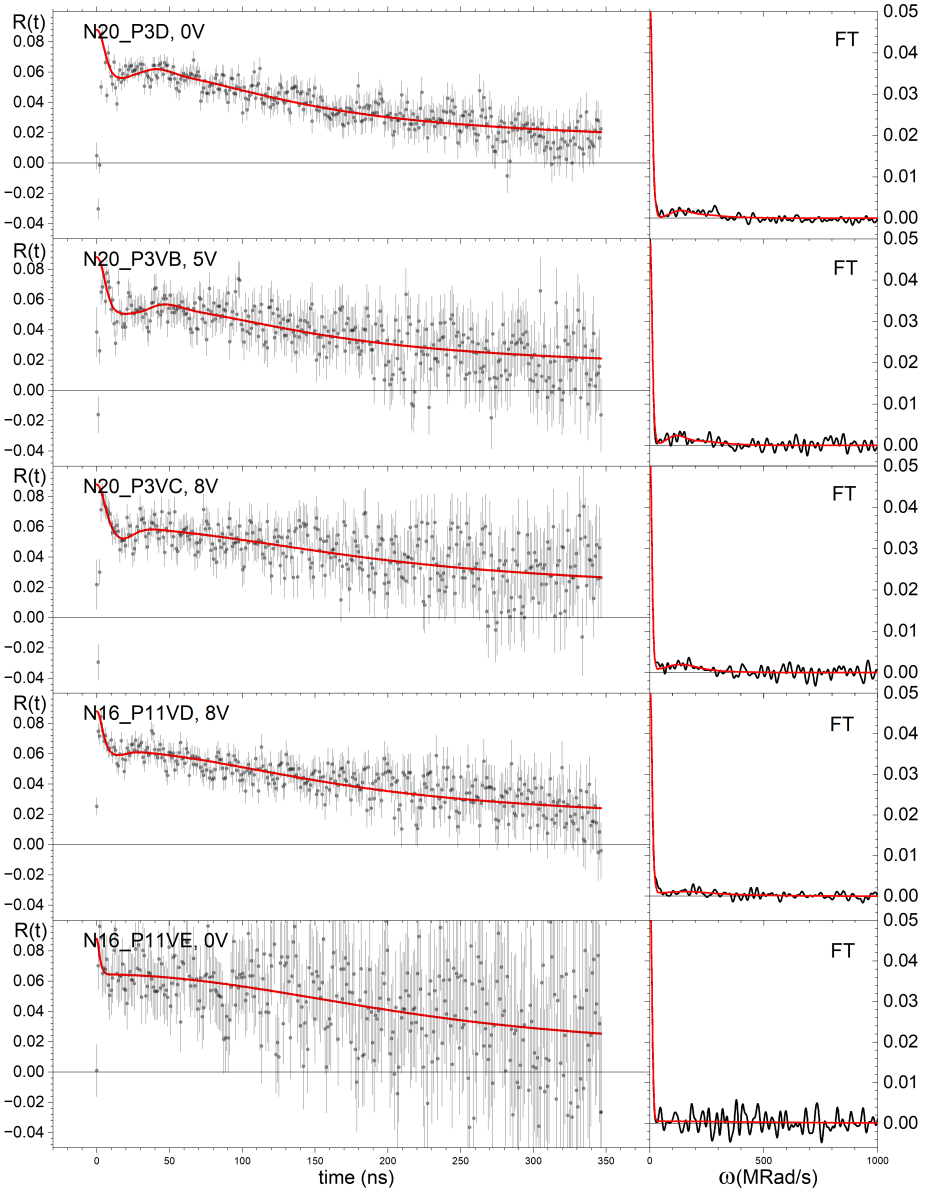

Figure 13: Results of Sample N20_P3 and N16_P11

	ω_0 [Mrad/s]	η	$\lvert V_{zz}\rvert$ [V/Å^2]	σ [Mrad/s]	f%
N20_P3D, 293K, 0V					
EFG 1	3.75(9)	~ 0	2.5(1)	3.7(3)	65(2)
EFG 2	113(6)	0.38(9)	77(5)	37(4)	35(1)
N20_P3VB, 293K, 5V					
EFG 1	3.4(2)	~ 0	2.3(1)	3.3(3)	58(3)
EFG 2	106(8)	0.2(1)	72(6)	37(8)	42(1)
N20_P3VC, 293K, 8V					
EFG 1	2.5(1)	~ 0	1.7(1)	2.8(3)	57(3)
EFG 2	89(8)	0.6(1)	61(6)	45(9)	43(2)
N20_P11B, 293K, 0V					
EFG 1	4.2(1)	~ 0	2.8(1)	4.7(2)	57(2)
EFG 2	139(9)	0.44(8)	95(7)	47(5)	43(2)
N20_P11VB, 293K, 6V					
EFG 1	4.3	~ 0	2.0(2)	6.3(5)	46(2)
EFG 2	160(13)	0.0(3)	109(10)	72(11)	54(3)
N20_P11VD, 293K, 0V					
EFG 1	3.2(1)	~ 0	2.2(1)	4.8(2)	46(1)
EFG 2	124(6)	0.42(6)	85(5)	61(7)	54(2)
N16_P11VD, 293K, 8V					
EFG 1	2.82(9)	~ 0	1.9(1)	3.2(2)	62
EFG 2	131(14)	0.3(1)	90(10)	85(15)	38(1)
N16_P11VE, 293K, 0V					
EFG 1	2.7(1)	~ 0	1.8(1)	2.0(3)	66(4)
EFG 2	168(27)	0(2)	115(19)	335(56)	34(1)

Table 1: Summary of results for old design

8.2 "new" design samples

Figure 9 depicts the R(t) spectra associated with the sample denoted as FFSSA. These spectra were acquired under varying experimental conditions. The initial spectrum corresponds to measurements taken prior to the application of any voltage, while the second spectrum was captured during the application of the forming voltage with the value of 60 V, and the third spectrum represents measurements taken subsequent to voltage application for V = 0. In the case of samples designed with the new configuration, EDX measurements did not reveal the presence of silver sulfide. Consequently, we employed a two fraction fitting approach for the analysis. The first fraction contributes significantly, ranging from 49% to 73% of the overall spectrum and corresponnds to ions implanted in TiO_2. It is noteworthy that the angular frequency (ω_0) for this fraction exhibited values of 232 Mrad/s before voltage application, 206 Mrad/s during voltage application, and 196 Mrad/s after voltage application. This fraction also displays substantial damping, with σ values spanning from 60 to 90 Mrad/s. The second fraction bears resemblance to the fraction observed in the old sample design, which corresponds to pure silver. However, it exhibits a diminished contribution, consistent with the expectation that the proportion of implanted ions within the silver matrix is reduced in the new design. It is important to note that there are discernible differences between the spectrum acquired prior to voltage application and the spectrum obtained after voltage was applied.

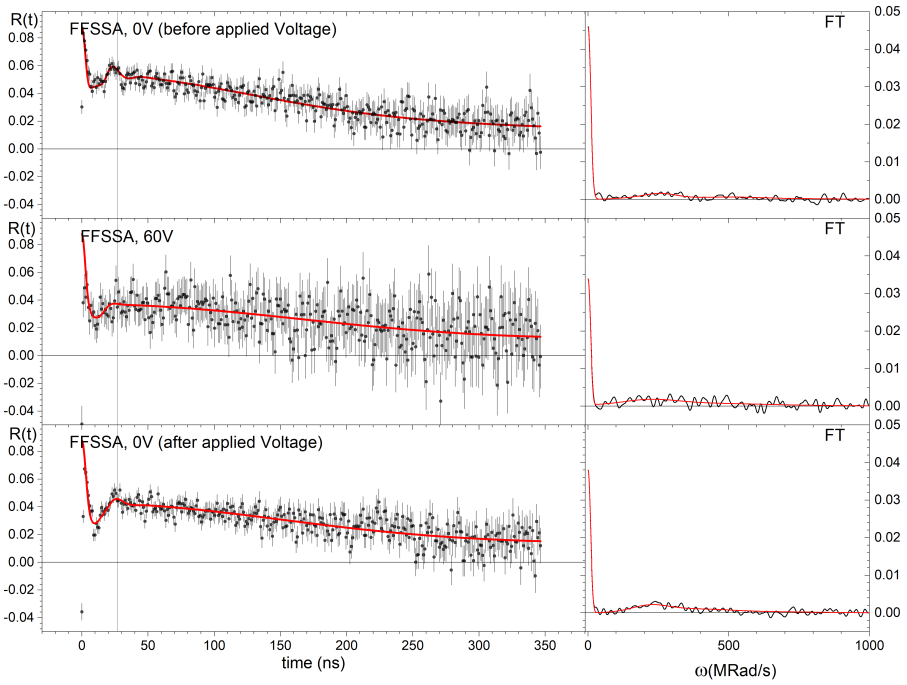

Figure 14: Results of Sample FFSSA

	ω_0 [Mrad/s]	η	$\lvert V_{zz}\rvert$ [V/Å^2]	σ [Mrad/s]	f%
FFSSA2, 293K, 0V					
EFG 1	232(26)	0.20(6)	159(18)	67(14)	49(2)
EFG 2	3.8(1)	~ 0	2.6(1)	2.0(2)	51(2)
FFSSA2VA, 293K, 60V					
EFG 1	206(16)	0.25(4)	141(12)	90(8)	73(6)
EFG 2	4.1(3)	~ 0	2.8(2)	1.1(7)	27(2)
FFSSA5VA, 293K, 0V					
EFG 1	196(7)	0.35(1)	134(7)	60(6)	67(2)
EFG 2	3.8(1)	~ 0	2.6(1)	1.3(2)	33(0)

Table 2: Summary of results for new design

9 Conclusions and Further Discussion

The presence of a silver sulfur layer detected on the contact pads of the old design samples underscores the importance of meticulously controlling the aging and storage conditions of these samples to optimize the analysis of the Perturbed Angular Correlation (PAC) spectrum.
Upon examination of an image of the sample holder, wherein a small white sheet of paper was employed to mark the beam spot, we have reached the conclusion that the region within the new design samples where ion channels are expected to form has either not been adequately implanted with cadmium ions or the implantation has been insufficient. Furthermore, it is improbable that ion channel formation is responsible for the observed changes in the spectrum, as such formations are not anticipated to occur at the contact pads.
An alternative explanation for the observed spectral variations could be attributed to the temperature rise between the electrodes as voltage is applied, leading to alterations in the surrounding crystal structure and subsequently affecting the distribution of the electric field gradient.
Another possibility to consider is the relatively short half-life of under 50 minutes for the three experiments conducted. The first of these experiments was conducted based on the initial implantation, while the second and third experiments were conducted following a separate implantation. Despite meticulous sample placement, even minimal variations in positioning could result in observable differences in the spectrum.
Furthermore, it is worth noting that even if the gap between the electrodes were to be implanted, the radioactive activity from implanted ^{111m}Cd within this region is insufficient to generate a statistically significant PAC spectrum.
Alternatively, we propose an alternative test device, initially suggested by Jens Röder, a consultant engaged in the course of these experiments. The current samples exhibit a notably small active zone wherein potential ion filaments are formed. Expanding the surface area increases the likelihood of a substantial number of probes coming to rest in close proximity to ion channels. To address this requirement, we propose an architectural configuration composed of gold, silver, titanium dioxide (TiO_2), and platinum layers, as depicted in Figure 15. Notably, the area of these layers can theoretically be scaled up, rendering it conducive to PAC experiments.
Gold is selected as a material to prevent any sulfidation of the silver layers. Implantation can be precisely executed by finely adjusting the beam energy in accordance with the thickness of the gold and silver layers, ensuring that a majority of the ions come to rest within the TiO_2 layer. Opting for indium ions as probes offers the advantage of enabling multiple experiments with the same implantation due to its significantly longer half-life of 2.8 days compared to cadmium.
Figure 16 presents a simulation depicting the penetration depth of a 50 keV ^{111}In beam, illustrating the efficacy of this setup. Another advantage of this configuration is the potential elimination of surface effects associated with the TiO_2 layer. It is imperative to underscore that this device is presently a hy-

pothetical concept, and further investigation is required to ascertain whether memristive properties manifest within this architecture and to identify suitable layer areas for experimentation.

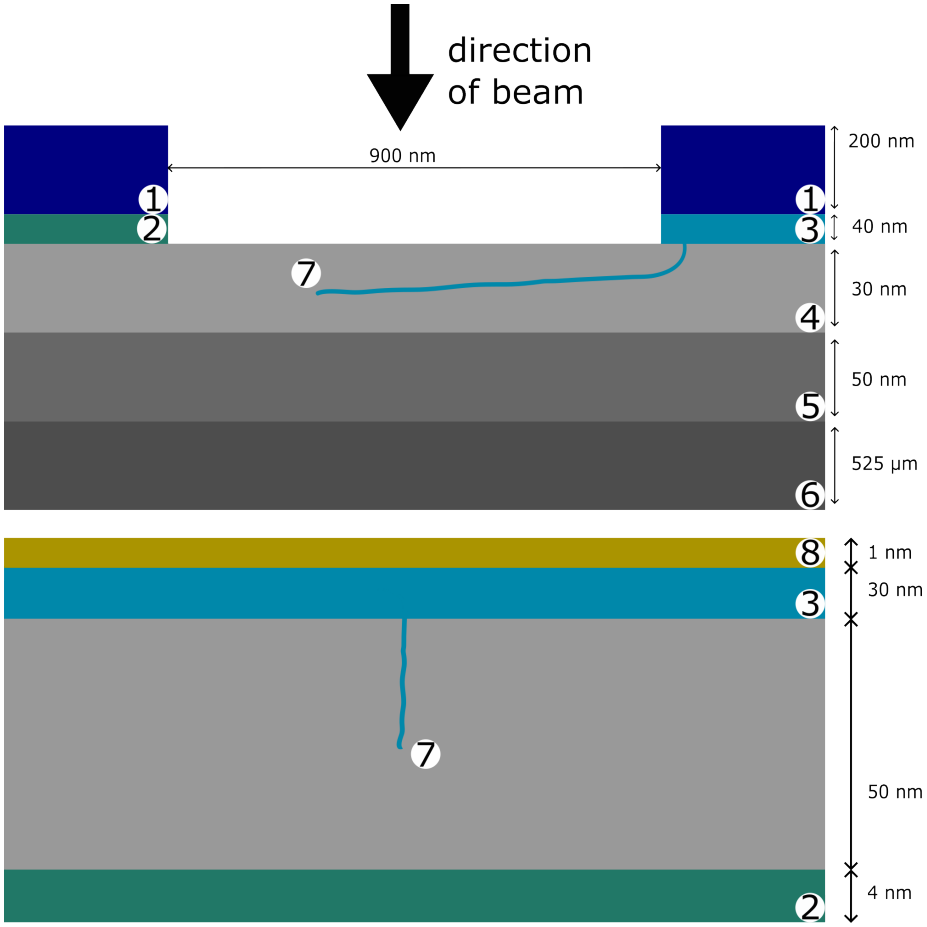

Figure 15: Architecture studied in this work (top) and new proposed architecture. 1: Ag coating, 2: Pt electrode, 3: Ag electrode, 4: TiO_2, 5: SiO_2, 6. Si, 7: Ag^+ ion channel, 8: Au corrosion protection (not correct proportions)

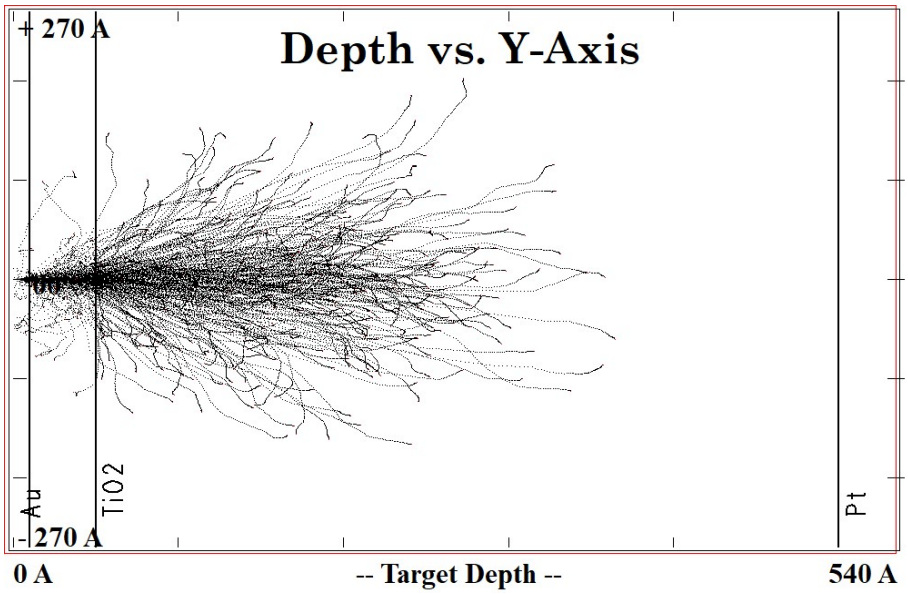

Figure 16: SRIM Simulation or new based on above dimensions of new architecture

References

[1] Marcelo Barbosa. *Implementation of "ab initio" Perturbed Angular Correlation Observables for Analysis of Fluctuating Quadrupole Interactions*. 2010.

[2] Sumanto Chanda. *How do we deduce the vector potential for a constant magnetic field?* Physics Stack Exchange. 2018. URL: https://physics.stackexchange.com/q/442523.

[3] L. Chua. "Memristor-The missing circuit element". In: *IEEE Transactions on Circuit Theory* 18.5 (1971), pp. 507–519. DOI: 10.1109/TCT.1971.1083337.

[4] Leon Chua, Georgios Ch Sirakoulis, and Andrew Adamatzky. *Handbook of Memristor Networks*. Springer Nature, 2019.

[5] Javier Del Valle et al. "Challenges in materials and devices for resistive-switching-based neuromorphic computing". In: *Journal of Applied Physics* 124.21 (2018).

[6] PAN Feng et al. "Nonvolatile resistive switching memories-characteristics, mechanisms and challenges". In: *Progress in Natural Science: Materials International* 20 (2010), pp. 1–15.

[7] J.P. Franey, G.W. Kammlott, and T.E. Graedel. "The corrosion of silver by atmospheric sulfurous gases". In: *Corrosion Science* 25.2 (1985), pp. 133–143. DOI: https://doi.org/10.1016/0010-938X(85)90104-0.

[8] A. Weidinger G. Schatz. *Nukleare Festkörperphysik*. B.G. Teubner, 1992.

[9] "J .G. Correia for GFIT19 and N. P. Barradas for NNFIT programs (PAC MANual Lisbon 1992".

[10] Oleg Kononchuk and B-Y Nguyen. *Silicon-on-insulator (soi) technology: Manufacture and applications*. Elsevier, 2014.

[11] Armandia Maria Lima Lopes. "Local prope studies on lattice distortions and electronic correlations in CMR Manganites". PhD thesis. Universidade de Aveiro, 2006.

[12] Wei Lu et al. "Electrochemical metallization cells—blending nanoionics into nanoelectronics?" In: *MRS bulletin* 37.2 (2012), pp. 124–130.

[13] Anton A Minnekhanov et al. "On the resistive switching mechanism of parylene-based memristive devices". In: *Organic Electronics* 74 (2019), pp. 89–95.

[14] Baker Mohammad et al. "State of the art of metal oxide memristor devices". In: *Nanotechnology Reviews* 5.3 (2016), pp. 311–329.

[15] M.A. Nagl et al. "A new tool for the search of nuclides with properties suitable for nuclear solid state physics based on the Evaluated Nuclear Structure Data Files". In: *Nuclear Instruments and Methods in Physics Research Section A: Accelerators, Spectrometers, Detectors and Associated Equipment* 726 (2013), pp. 17–30. DOI: https://doi.org/10.1016/j.nima.2013.05.045.

[16] Yu V Pershin and Massimiliano Di Ventra. "Spin memristive systems: Spin memory effects in semiconductor spintronics". In: *Physical Review B* 78.11 (2008), p. 113309.

[17] Dmitri B Strukov et al. "The missing memristor found". In: *nature* 453.7191 (2008), pp. 80–83.

[18] David Varghese and Gaurav Gandhi. "Memristor based high linear range differential pair". In: *2009 International Conference on Communications, Circuits and Systems*. IEEE. 2009, pp. 935–938.

[19] Th. Wichert and E. Recknagel. "Perturbed Angular Correlation". In: *Microscopic Methods in Metals*. Ed. by Ulrich Gonser. Springer Berlin Heidelberg, 1986, pp. 317–364. DOI: 10.1007/978-3-642-46571-0_11.

[20] J Joshua Yang, Dmitri B Strukov, and Duncan R Stewart. "Memristive devices for computing". In: *Nature nanotechnology* 8.1 (2013), pp. 13–24.

[21] Ian Yap. *A particular EFG temperature dependence for 181(TiO2): An electron-gamma TDPAC study*. 2022.

[22] Xumeng Zhang et al. "An artificial neuron based on a threshold switching memristor". In: *IEEE Electron Device Letters* 39.2 (2017), pp. 308–311.

[23] Ivana Zrinski et al. "Influence of electrolyte selection on performance of tantalum anodic oxide memristors". In: *Applied Surface Science* 565 (2021), p. 150608.

10 Acknowledgement

The research leading to these results has received funding from the European Union's Horizon Europe research and innovation programme under grant agreement no. 101057511
I would like to express my sincere gratitude to several individuals who have played instrumental roles in the successful completion of this research project.
First and foremost, I extend my heartfelt thanks to Dr. Adeleh Mokhles Gerami and Dr. Juliana Schell for their invaluable guidance and mentorship during my tenure as a summer student at CERN. Their expertise, support, and encouragement have been pivotal in shaping the trajectory of my time as a summer student.
I am deeply indebted to Dr. João Guilherme Martins Correia, whose generosity in dedicating a significant amount of his time to assist me with various facets of my summer student program has been immeasurable. His mentorship and willingness to share knowledge have made a profound impact on my academic journey.
I would also like to express my appreciation to all the fellow summer students who provided me with advice and shared their insights. Your camaraderie and collaborative spirit have enriched my experience at CERN and contributed to the overall success of this endeavor.
This work would not have been possible without the support and contributions of these remarkable individuals, and for that, I am truly grateful.